A finite element method for the resolution of the Reduced Navier-Stokes/Prandtl equations

Gabriel R. Barrenechea, Franz Chouly

A finite element method for the resolution of the Reduced Navier-Stokes/Prandtl equations

Gabriel R. Barrenechea[1] and Franz Chouly[2]

[1] Dept. of Mathematics, University of Strathclyde, 26 Richmond Street, Glasgow G1 1XH, Scotland.
grb@maths.strath.ac.uk
[2] INRIA, REO team, Rocquencourt - BP 105, 78153 Le Chesnay Cedex, France.
franz.chouly@inria.fr

August 22, 2008

Abstract. A finite element method to solve the Reduced Navier-Stokes Prandtl (RNS/P) equations is described. These equations are an asymptotic simplification of the full Navier-Stokes equations, obtained when one dimension of the domain is of one order smaller than the others. These are therefore of particular interest to describe flows in channels or pipes of small diameter. A low order finite element discretization, based on a piecewise constant approximation of the pressure, is proposed and analyzed. Numerical experiments which consist in fluid flow simulations within a constricted pipe are provided. Comparisons with Navier-Stokes simulations allow to evaluate the performance of prediction of the finite element method, and of the model itself.

Keywords : incompressible flow, RNS/P equations, finite elements.

1 Introduction

For some kinds of flow problems, it is physically relevant to simplify the full Navier-Stokes equations assuming that one or two characteristic lengths are predominent. Among the most classical examples are the Prandtl's boundary layer equations (see e.g. [21]) or the hydrostatic approximation for shallow water flows (see e.g. [2]). The interest of these simplifications is a refined analysis of the fluid flow problem, through a better understanding of its relevant scalings. It can be also motivated by practical considerations, as it might reduce the computation cost far above those of the most efficient Navier-Stokes solvers, despite the considerable effort that has been made in this direction (see e.g. [25]).

For flows in long pipes of small diameter, such a simplification, justified by an asymptotic analysis, has been derived and called Reduced Navier-Stokes/Prandtl (RNS/P) equations [16]. These equations have been employed successfully to model various problems, specifically in the domain of biological flows: in a stenosis [16], in the laryngeal glottis [15], in the pharyngeal duct [26, 17]. In particular, the prediction of pressure and wall shear stress distributions has been compared to references such as Navier-Stokes simulations [17] or experimental measurements [26]. It results from these comparisons that the RNS/P predictions are quite close to the references, with a relative error of a few percents.

For these equations, a numerical method based on finite differences has been proposed and tested in [15]. It is a streamwise marching algorithm, inspired from the classical methods

designed to solve the heat equation [11]. Even if the proposed method is cheap and adaptable to some different geometries, it has some important drawbacks. Among them, we can quote:

– first, it lacks of robustness. Specifically, for some categories of geometries, such as constrictions, numerical problems occur after the separation of the flow. This is mostly due to recirculation effects, which cannot be easily taken into account in the finite differences framework. The standard method is to use the "FLARE" approximation [19] which consists in removing the $u\partial_x u$ term when the longitudinal velocity is negative [16]. However, this is an *ad-hoc* approximation and does not ensure a correct computation in the whole domain.
– Some care has to be taken when adapting a finite differences scheme to complicated geometries, or to a three-dimensional problem [5].
– If we are interested in fluid-structure interaction problems (such as in the upper airways [8]), with the finite element method for solving the motion of the structure, the transmission of the forces at the interface can not be done in a simple and natural way (see [8] for the details).

As a result of the previous considerations, in this work we are interested in the first steps towards a finite element method for the resolution of the RNS/P equations, which will avoid some of these disadvantages. Even if the presentation and the results are given for the bidimensional case, the method can be easily extended to the tridimensional case.

The plan of the paper is as follows. First, the complete boundary value problem is given in Section 2. The finite element method is described and analyzed in Section 3; in particular, since finite elements of common use for the Navier-Stokes equations - namely Taylor-Hood element [27] and the Mini element [11] - do not provide a correct approximation, we use a specific finite element, originally proposed in [23] for the Stokes equation. It is shown that with this method, the discrete problem admits a solution. Numerical experiments, presented in Section 4, have been carried out to confirm the analysis, and to test the precision of the method through comparison with Navier-Stokes simulations, taken as a reference. Finally some concluding remarks and perspectives are drawn.

2   The boundary value problem

The Reduced Navier-Stokes/Prandtl (RNS/P) equations are derived from the Navier-Stokes (1) equation. For the sake of simplicity, one can assume a newtonian, steady, incompressible, laminar and bidimensional flow:

$$\begin{cases} (\boldsymbol{u} \cdot \nabla)\, \boldsymbol{u} = -\frac{1}{\rho}\nabla p + \nu \triangle \boldsymbol{u} + \boldsymbol{g}, \\ \qquad \nabla \cdot \boldsymbol{u} = 0, \end{cases} \tag{1}$$

where $\boldsymbol{u}$ is the velocity, p is the pressure, ρ is the density, ν is the kinematic viscosity and $\boldsymbol{g}$ is the external force field; $\boldsymbol{g}$ is in a great amount of applications the gravity field but may also stand for any kind of other external influence (e.g. a magnetic field). To derive the RNS/P equations, we need two assumptions, namely:
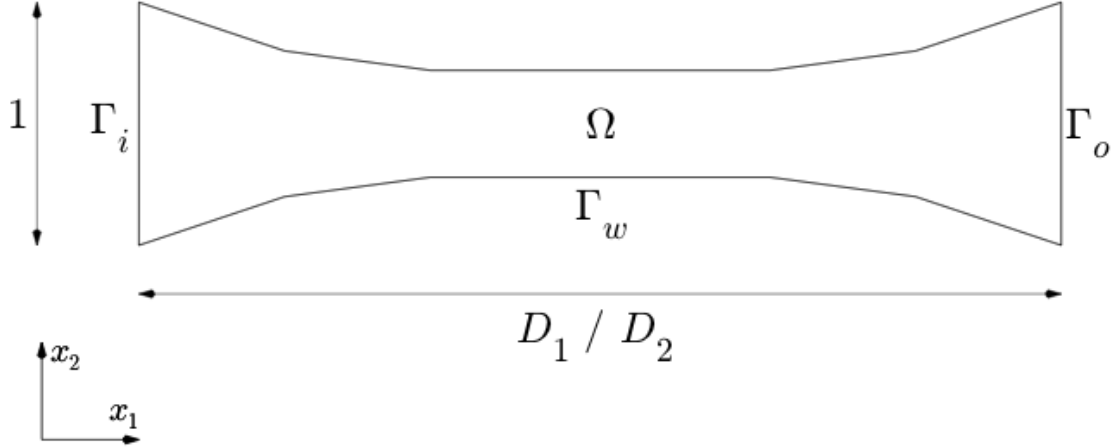
Fig. 1. The domain Ω for the resolution of the RNS/P equations, with the notations for the different parts of the boundary. Note that x_1 and x_2 are non-dimensional coordinates.

1. if we note D_2 the transversal dimension of the domain and D_1 the longitudinal dimension, then $D_1/D_2 \gg 1$ (Fig. 1).
2. if the Reynolds number is defined as $\mathrm{Re} = U_0 D_2/\nu$, where U_0 stands for the maximal velocity at the entry, then $\mathrm{Re} \gg 1$.

Then, the Navier-Stokes equation (1) can be simplified in order to obtain Reduced Navier-Stokes / Prandtl (RNS/P) equations (see [16] for the derivation):

$$\begin{cases} u_1\,\partial_{x_1}u_1 + u_2\,\partial_{x_2}u_1 = -\frac{1}{\rho}\partial_{x_1}p + \nu\,\partial_{x_2}^2 u_1 + g_1, \\ \qquad\qquad \partial_{x_2}p = 0, \\ \qquad \partial_{x_1}u_1 + \partial_{x_2}u_2 = 0. \end{cases} \tag{2}$$

Here, (u_1, u_2) are respectively the longitudinal and the transversal components of the velocity $\boldsymbol{u}$, and g_1 is the longitudinal component of the external force field $\boldsymbol{g}$. In the case of a gravity field, it means of course that the gravity is taken into account only if the duct is not horizontal. Boundary conditions consist of no slip on the lower and upper walls as well as an inlet flow at the entrance. The exit of the domain is considered as free. As a result, the RNS/P equations are the Prandtl boundary layer equations [7] with two major differences:

1. the domain in the RNS/P formulation is bounded in the transverse direction and there is no more fitting at the infinity with the inviscid flow;
2. the pressure distribution in the domain is an unknown.

Let us consider Ω which is a polygonal domain in $\mathbb{R}^2$ with boundary $\partial\Omega$; $\Gamma_i \subset \partial\Omega$ is the entry (inlet flow), $\Gamma_w \subset \partial\Omega$ is the rigid wall (with no-slip boundary conditions) and $\Gamma_o \subset \partial\Omega$ is the exit (outlet flow) (Fig. 1). We give now the full boundary value problem that aims to be solved, in a non-dimensional form:

3

$$\begin{cases} u_1 \, \partial_{x_1} u_1 + u_2 \, \partial_{x_2} u_1 + \partial_{x_1} p - \frac{1}{\mathrm{Re}} \, \partial_{x_2}^2 u_1 = g_1 & \text{in } \Omega, \\ \partial_{x_2} p = 0 & \text{in } \Omega, \\ \partial_{x_1} u_1 + \partial_{x_2} u_2 = 0 & \text{in } \Omega, \\ u_1 = u_1^0 & \text{on } \Gamma_i, \\ u_1 = 0 & \text{on } \Gamma_w, \\ u_2 \, n_2 = 0 & \text{on } \Gamma_i \cup \Gamma_w, \\ \boldsymbol{\sigma}_{\mathrm{RNSP}} \, \boldsymbol{n} = 0 & \text{on } \Gamma_o. \end{cases} \tag{3}$$

The velocity profile u_1^0 at the entry may be arbitrary, usually a flat profile or a Poiseuille profile. Note that the condition $u_2 \, n_2 = 0$ comes from the fact that u_2 is expected to be less regular than u_1 (as in [2]), so that the classical trace theorems (see e.g. [18]) do not allow to define u_2 on the boundary (in next section is introduced the space in which u_2 is defined). The condition on Γ_o is a "do-nothing" condition, where $\boldsymbol{\sigma}_{\mathrm{RNSP}} = -p \, \boldsymbol{I} + \frac{1}{\mathrm{Re}} \partial_{x_2} u_1 \, \boldsymbol{e_1} \otimes \boldsymbol{e_2}$ is a degenerated Cauchy stress tensor associated to the RNS/P equations, and $\boldsymbol{n}$ the normal unit vector oriented outward the domain.

3 The finite element method

As in the case of Stokes or Navier-Stokes equation, a finite element method can be proposed to solve the RNS/P equations. Moreover, some of the techniques already known to obtain a discrete approximation and to analyze it can be adapted to this case. Nevertheless, as in the case of the primitive equations of the ocean, in which the pressure is also constant in one direction of the space, finite elements such as Taylor-Hood or Mini element are inappropriate for discretization [1]. Hence, we propose a discretization using an element which was first studied in [23].

3.1 Weak formulation

To avoid technical difficulties, the problem (3) is rewritten with homogeneous Dirichlet boundary conditions on $\partial \Omega$ ($\Gamma_w = \partial \Omega$, $\Gamma_i = \emptyset, \Gamma_o = \emptyset$)[3]. Let us first present some notations. By $\mathcal{L}^2(\Omega)$ we denote the space of square integrable scalar functions on Ω, $(\cdot, \cdot)_\Omega$ stands for the inner product in $\mathcal{L}^2(\Omega)$ (in $\mathcal{L}^2(\Omega)^2$ or in $\mathcal{L}^2(\Omega)^{2\times2}$, if necessary); $||.||_{0,\Omega}$ stands for the norm in $\mathcal{L}^2(\Omega)$ associated to $(\cdot, \cdot)_\Omega$. $\mathcal{L}_0^2(\Omega)$ is the subspace of functions in $\mathcal{L}^2(\Omega)$ with zero mean value on Ω. $\mathcal{H}^1(\Omega)$ is the space of square integrable scalar functions on Ω, with square integrable first derivatives. In the sequel, we will need the following space

$$\mathcal{H}^1(\partial_{x_2}, \Omega) = \{v \in \mathcal{L}^2(\Omega) \mid \partial_{x_2} v \in \mathcal{L}^2(\Omega)\}. \tag{4}$$

$\mathcal{H}_0^1(\Omega)$ stands for the closed subspace of $\mathcal{H}^1(\Omega)$ with vanishing trace on $\partial \Omega$. Similarly, we note $\mathcal{H}_0^1(\partial_{x_2}, \Omega)$ the following space:

---

[3] However, the weak formulation in the general case will be given in the next remark.

$$\mathcal{H}_0^1(\partial_{x_2}, \Omega) = \{v \in \mathcal{H}^1(\partial_{x_2}, \Omega) \mid vn_2|_{\partial\Omega} = 0\}. \tag{5}$$

$\boldsymbol{H^1}(\Omega)$, $\boldsymbol{H}(\Omega)$ and $\boldsymbol{H_0}(\Omega)$ are the following spaces of vector-valued functions:

$$\begin{aligned}
\boldsymbol{H^1}(\Omega) &= \mathcal{H}^1(\Omega) \times \mathcal{H}^1(\Omega), \\
\boldsymbol{H}(\Omega) &= \mathcal{H}^1(\Omega) \times \mathcal{H}^1(\partial_{x_2}, \Omega), \\
\boldsymbol{H_0}(\Omega) &= \mathcal{H}_0^1(\Omega) \times \mathcal{H}_0^1(\partial_{x_2}, \Omega).
\end{aligned} \tag{6}$$

$\boldsymbol{H^1}(\Omega)$ is a Hilbert space with the following scalar product:

$$(\boldsymbol{u}, \boldsymbol{v})_{1,\Omega} = (\boldsymbol{u}, \boldsymbol{v})_\Omega + (\nabla\boldsymbol{u}, \nabla\boldsymbol{v})_\Omega. \tag{7}$$

$\boldsymbol{H}(\Omega)$ is also a Hilbert space with the scalar product:

$$(\boldsymbol{u}, \boldsymbol{v})_{\boldsymbol{H}(\Omega)} = (\boldsymbol{u}, \boldsymbol{v})_\Omega + (\nabla u_1, \nabla v_1)_\Omega + (\partial_{x_2} u_2, \partial_{x_2} v_2)_\Omega. \tag{8}$$

This implies the following property on the norms:

$$\forall \boldsymbol{v} \in \boldsymbol{H^1}(\Omega), \ ||\boldsymbol{v}||_{\boldsymbol{H}(\Omega)} \leq ||\boldsymbol{v}||_{1,\Omega}, \tag{9}$$

with $||.||_{1,\Omega}$ the norm on $\boldsymbol{H^1}(\Omega)$ associated to $(\cdot, \cdot)_{1,\Omega}$. Moreover, let us note $c(\cdot, \cdot, \cdot)$, $a_{\text{Re}}(\cdot, \cdot)$, $a_\lambda(\cdot, \cdot)$ and $a(\cdot, \cdot)$ the continuous trilinear and bilinear forms on $\boldsymbol{H_0}(\Omega)$ defined by:

$$\begin{aligned}
c &: (\boldsymbol{u}, \boldsymbol{v}, \boldsymbol{w}) \longmapsto (u_1\, \partial_{x_1} v_1 + u_2\, \partial_{x_2} v_1, w_1)_\Omega, \\
a_{\text{Re}} &: (\boldsymbol{u}, \boldsymbol{v}) \longmapsto \tfrac{1}{\text{Re}}(\partial_{x_2} u_1, \partial_{x_2} v_1)_\Omega, \\
a_\lambda &: (\boldsymbol{u}, \boldsymbol{v}) \longmapsto (\lambda \nabla \cdot \boldsymbol{u}, \nabla \cdot \boldsymbol{v})_\Omega, \\
a &: (\boldsymbol{u}, \boldsymbol{v}) \longmapsto a_{\text{Re}}(\boldsymbol{u}, \boldsymbol{v}) + a_\lambda(\boldsymbol{u}, \boldsymbol{v}).
\end{aligned} \tag{10}$$

Here, λ is a non-negative (possibly equal to zero) scalar field over Ω. The least-squares term a_λ can be added into the variational formulation without affecting the solution. Although irrelevant for the continuous problem, this least-squares term has been introduced as a standard stabilization for convection-dominated flow problems (see, e.g., [4] for a recent review on this issue) an has an effect on the solution of the discrete problem (see Section 4 for a discussion). We also introduce the continuous bilinear form $b(\cdot, \cdot) : \mathcal{L}_0^2(\Omega) \times \boldsymbol{H_0}(\Omega) \to \mathbb{R}$ defined by:

$$b : (p, \boldsymbol{v}) \longmapsto -(p, \nabla \cdot \boldsymbol{v})_\Omega. \tag{11}$$

Using these forms, we present the following weak formulation for (3): *Find $(\boldsymbol{u}, p) \in \boldsymbol{H_0}(\Omega) \times \mathcal{L}_0^2(\Omega)$ such that:*

$$\begin{cases}
\forall \boldsymbol{v} \in \boldsymbol{H_0}(\Omega), \quad c(\boldsymbol{u}, \boldsymbol{u}, \boldsymbol{v}) + a(\boldsymbol{u}, \boldsymbol{v}) + b(p, \boldsymbol{v}) = (\boldsymbol{g}, \boldsymbol{v})_\Omega, \\[2mm]
\forall q \in \mathcal{L}_0^2(\Omega), \qquad\qquad\qquad\qquad\qquad b(q, \boldsymbol{u}) = 0.
\end{cases} \tag{12}$$

Note that from the boundary value problem, we have $\boldsymbol{g} = (g_1, 0)$. Nevertheless, we will consider the general case $g_2 \neq 0$ in the rest of the text.

Remark. In the case of non-homogeneous boundary conditions, the weak formulation (12) is still valid with the following modifications: $\boldsymbol{u}$ belongs to $\boldsymbol{H_{\Gamma_w}}(\Omega)$, the subspace of functions

in $\boldsymbol{H}(\Omega)$ for which trace vanishes on Γ_w. The inlet flow is imposed by setting u_1 equal to u_1^0 on Γ_i. The test function $\boldsymbol{v}$ belongs to $\boldsymbol{H}_{\Gamma_w \cup \Gamma_i}(\Omega)$ since the "do-nothing" condition is chosen for the outlet flow on Γ_o. Due to this condition, the functions p and q are not restricted to $\mathcal{L}_0^2(\Omega)$ and are now in $\mathcal{L}^2(\Omega)$. $\square$

We now return to the case of homogeneous Dirichlet condition for the analysis of the problem, and we introduce the following space:

$$\boldsymbol{H_b}(\Omega) \overset{\text{DEF}}{=} \ker b = \{\boldsymbol{v} \in \boldsymbol{H_0}(\Omega) \,|\, \forall q \in \mathcal{L}_0^2(\Omega), \, b(q, \boldsymbol{v}) = 0\} = \{\boldsymbol{v} \in \boldsymbol{H_0}(\Omega) \,|\, \nabla \cdot \boldsymbol{v} = 0\}, \quad (13)$$

where the last equality arises from the fact that $\nabla \cdot \boldsymbol{v} \in \mathcal{L}_0^2(\Omega)$. As for the Navier-Stokes and Stokes equations, we reformulate this mixed weak formulation into two dependent problems. For stability reasons (see Lemma 2 below), the convective term $c(\cdot, \cdot, \cdot)$ is transformed using the following well-known relationship:

$$\forall \boldsymbol{u}, \boldsymbol{v}, \boldsymbol{w} \in \boldsymbol{H_0}(\Omega), \ c_{\mathrm{s}}(\boldsymbol{u}, \boldsymbol{v}, \boldsymbol{w}) = -\frac{1}{2}(\nabla \cdot \boldsymbol{u}, v_1 w_1)_\Omega. \quad (14)$$

As a result, $c_{\mathrm{s}}(\cdot, \cdot, \cdot)$, the symmetric part of $c(\cdot, \cdot, \cdot)$, vanishes on $\boldsymbol{H_b}(\Omega)$ and the trilinear form is equal to its antisymmetric part:

$$\begin{aligned} &\forall \boldsymbol{u}, \boldsymbol{v}, \boldsymbol{w} \in \boldsymbol{H_b}(\Omega), \\ &c(\boldsymbol{u}, \boldsymbol{v}, \boldsymbol{w}) = c_{\mathrm{a}}(\boldsymbol{u}, \boldsymbol{v}, \boldsymbol{w}) = \tfrac{1}{2}\left((u_1 \, \partial_{x_1} v_1 + u_2 \, \partial_{x_2} v_1, w_1)_\Omega - (u_1 \, \partial_{x_1} w_1 + u_2 \, \partial_{x_2} w_1, v_1)_\Omega\right). \end{aligned} \quad (15)$$

Using (14)-(15) we can propose the following equivalent formulation for the problem (12):

− Find $\boldsymbol{u} \in \boldsymbol{H_b}(\Omega)$ such that :

$$\forall \boldsymbol{v} \in \boldsymbol{H_b}(\Omega), \quad c_{\mathrm{a}}(\boldsymbol{u}, \boldsymbol{u}, \boldsymbol{v}) + a(\boldsymbol{u}, \boldsymbol{v}) = (\boldsymbol{g}, \boldsymbol{v})_\Omega, \quad (16)$$

− Find $p \in \mathcal{L}_0^2(\Omega)$ such that :

$$\forall \boldsymbol{v} \in \boldsymbol{H_0}(\Omega), \quad b(p, \boldsymbol{v}) = (\boldsymbol{g}, \boldsymbol{v})_\Omega - c_{\mathrm{a}}(\boldsymbol{u}, \boldsymbol{u}, \boldsymbol{v}) - a(\boldsymbol{u}, \boldsymbol{v}). \quad (17)$$

3.2 Finite element spaces

For the continuous problem (16)-(17), a discretization first proposed in [23] for the Stokes problem has been chosen: a discontinuous approximation of the pressure is preferred as it provides local conservation of the mass (cf. [13]). Let $\{\mathcal{T}_h\}_{h>0}$ be a regular family of admissible triangulations of Ω (cf. [11]). For each $K \in \mathcal{T}_h$, h_K stands for the element diameter and $h = \max_{(K \in \mathcal{T}_h)} h_K$. The following space has been chosen for the velocity field:

$$\boldsymbol{H_h} = (H_{h,2} \cap \mathcal{H}_0^1(\Omega)) \times (H_{h,1} \cap \mathcal{H}_0^1(\partial_{x_2}, \Omega)), \quad (18)$$

where, for $k = 1, 2$:

$$H_{h,k} = \{v \in \mathcal{C}^0(\bar{\Omega}) \,|\, \forall K \in \mathcal{T}_h, \, v|_K \in \mathbb{P}_k(K)\}. \quad (19)$$

6

We also need to introduce the space $\boldsymbol{H_{h,b}}$, defined as follows:

$$\boldsymbol{H_{h,b}} = \{\boldsymbol{v_h} \in \boldsymbol{H_h} \,|\, \forall q_h \in \Pi_h, \, b(q_h, \boldsymbol{v_h}) = 0\}. \tag{20}$$

We note that $\boldsymbol{H_{h,b}}$ is not necessarily a subspace of $\boldsymbol{H_b}(\Omega)$. The pressure is approximated using the following space:

$$\Pi_h = \{q \in \mathcal{L}_0^2(\Omega) \,|\, \forall K \in \mathcal{T}_h, \, q|_K \in \mathbb{P}_0(K)\}. \tag{21}$$

The finite element associated to this choice is called $\mathbb{P}_2/\mathbb{P}_1/\mathbb{P}_0$. Using this pair of spaces, we propose the following finite element method for (16)-(17):

- Find $\boldsymbol{u_h} \in \boldsymbol{H_{h,b}}$ such that:

$$\forall \boldsymbol{v_h} \in \boldsymbol{H_{h,b}}, \quad c_{\mathrm{a}}(\boldsymbol{u_h}, \boldsymbol{u_h}, \boldsymbol{v_h}) + a(\boldsymbol{u_h}, \boldsymbol{v_h}) = (\boldsymbol{g}, \boldsymbol{v_h})_\Omega. \tag{22}$$

- Find $p_h \in \Pi_h$ such that:

$$\forall \boldsymbol{v_h} \in \boldsymbol{H_h}, \quad b(p_h, \boldsymbol{v_h}) = (\boldsymbol{g}, \boldsymbol{v_h})_\Omega - c_{\mathrm{a}}(\boldsymbol{u_h}, \boldsymbol{u_h}, \boldsymbol{v_h}) - a(\boldsymbol{u_h}, \boldsymbol{v_h}). \tag{23}$$

3.3 Analysis of the discrete problem

The aim of this section is to analyze the discrete problem (22)-(23). It will be proved that it admits at least one solution. We start with the following technical, but fundamental result:

Lemma 1. *The mapping*

$$\begin{aligned} ||.||_{\mathrm{x}_2} : \quad &\boldsymbol{H_{h,b}} \quad \longrightarrow \mathbb{R} \\ &\boldsymbol{v_h} = (v_{h,1}, v_{h,2}) \longmapsto ||\boldsymbol{v_h}||_{\mathrm{x}_2} = ||\partial_{x_2} v_{h,1}||_{0,\Omega}, \end{aligned} \tag{24}$$

defines a norm on $\boldsymbol{H_{h,b}}$.

Proof. The only property to check is that $||\boldsymbol{v_h}||_{\mathrm{x}_2} = 0$ implies $\boldsymbol{v_h} = \boldsymbol{0}$ in Ω. The other properties arise directly from the fact that $||.||_{0,\Omega}$ is a norm on $\mathcal{L}^2(\Omega)$. Let us consider $\boldsymbol{v_h} \in \boldsymbol{H_{h,b}}$ such that $||\boldsymbol{v_h}||_{\mathrm{x}_2} = 0$. The Poincaré inequality (see [18])

$$||v_{h,1}||_{0,\Omega} \leq C(\Omega) \, ||\partial_{x_2} v_{h,1}||_{0,\Omega}, \tag{25}$$

implies that $v_{h,1} = 0$ in Ω. As a result, $v_{h,2}$ satisfies

$$\forall q_h \in \Pi_h, \, (q_h, \partial_{x_2} v_{h,2})_\Omega = 0. \tag{26}$$

Let us now remark that the function $v_{h,2}$ can be written as follows on each triangle K_i of the mesh:

$$v_{h,2}|_{K_i}(x_1, x_2) = \alpha_i + \beta_i x_1 + \gamma_i x_2. \tag{27}$$

For two given elements K_i and K_j of the mesh, the function

$$\tilde{q}_h = \frac{1}{|K_i|} \mathbb{1}_{K_i} - \frac{1}{|K_j|} \mathbb{1}_{K_j}, \tag{28}$$

7

belongs to Π_h, and then, using (26) we easily see that

$$\gamma_i = \gamma_j. \tag{29}$$

Let $\mathcal{D} = \{(x_1^0, x_2) \mid x_2 \in \mathbb{R}\}$ be a vertical line, for any arbitrary x_1^0 such that $\mathcal{D} \cap \Omega \neq \emptyset$. This line intersects the mesh in a sequence of adjacent triangles $(K_i)_{i \in \{0,\dots,n\}}$. The property (29) and the continuity of $v_{h,2}$ imply that:

$$\forall i \in \{0, \dots, n\}, \ \alpha_i = \alpha_0, \ \beta_i = \beta_0, \ \gamma_i = \gamma_0. \tag{30}$$

The boundary conditions that satisfies $v_{h,2}$ are then such that: $\alpha_0 = \beta_0 = \gamma_0 = 0$. Since the same argument may be used for every (or almost every) x_1^0 such that $\mathcal{D} \cap \Omega \neq \emptyset$, then $\boldsymbol{v}_h = \boldsymbol{0}$ in Ω. $\square$

Remark. A consequence of this lemma is that $(\boldsymbol{H}_{h,b}, (\cdot, \cdot)_{x_2})$ is a Hilbert space with the scalar product : $(\boldsymbol{u}_h, \boldsymbol{v}_h)_{x_2} = (\partial_{x_2} u_{h,1}, \partial_{x_2} v_{h,1})_\Omega.$ $\square$

Lemma 2. *For $\lambda \geq 0$, the problem (22) admits at least one solution $\boldsymbol{u}_h \in \boldsymbol{H}_{h,b}$.*

Proof. We follow an approach similar to the one presented in [24] for the full Navier-Stokes equations. In $(\boldsymbol{H}_{h,b}, (\cdot, \cdot)_{x_2})$, finite dimensional Hilbert space, we introduce the mapping f from $\boldsymbol{H}_{h,b}$ into itself as follows. For $\boldsymbol{v}_h \in \boldsymbol{H}_{h,b}$, $f(\boldsymbol{v}_h)$ is the unique vector such that:

$$\forall \boldsymbol{w}_h \in \boldsymbol{H}_{h,b}, \quad (f(\boldsymbol{v}_h), \boldsymbol{w}_h)_{x_2} = c_a(\boldsymbol{v}_h, \boldsymbol{v}_h, \boldsymbol{w}_h) + a(\boldsymbol{v}_h, \boldsymbol{w}_h) - (\boldsymbol{g}, \boldsymbol{w}_h)_\Omega. \tag{31}$$

It is easy to check that f is a continuous mapping. Now, for $\lambda \geq 0$, $a(\cdot, \cdot)$ satisfies

$$\forall \boldsymbol{v}_h \in \boldsymbol{H}_{h,b}, \quad a(\boldsymbol{v}_h, \boldsymbol{v}_h) \geq \frac{1}{\mathrm{Re}} ||\boldsymbol{v}_h||_{x_2}^2, \tag{32}$$

and, using the Cauchy-Schwarz inequality and the equivalence of norms in a finite dimensional space there exists a positive constant $C_{1,h}$ such that:

$$\forall \boldsymbol{v}_h \in \boldsymbol{H}_{h,b}, \ |(\boldsymbol{g}, \boldsymbol{v}_h)_\Omega| \leq C_{1,h} \, ||\boldsymbol{g}||_{0,\Omega} \, ||\boldsymbol{v}_h||_{x_2}. \tag{33}$$

Using the previous results, f satisfies

$$
\begin{aligned}
(f(\boldsymbol{v}_h), \boldsymbol{v}_h)_{x_2} &= c_a(\boldsymbol{v}_h, \boldsymbol{v}_h, \boldsymbol{v}_h) + a(\boldsymbol{v}_h, \boldsymbol{v}_h) - (\boldsymbol{g}, \boldsymbol{v}_h)_\Omega \\
&= a(\boldsymbol{v}_h, \boldsymbol{v}_h) - (\boldsymbol{g}, \boldsymbol{v}_h)_\Omega \\
&\geq \tfrac{1}{\mathrm{Re}} ||\boldsymbol{v}_h||_{x_2}^2 - C_{1,h} \, ||\boldsymbol{g}||_{0,\Omega} \, ||\boldsymbol{v}_h||_{x_2} \\
&\geq ||\boldsymbol{v}_h||_{x_2} \left(\tfrac{1}{\mathrm{Re}} ||\boldsymbol{v}_h||_{x_2} - C_{1,h} \, ||\boldsymbol{g}||_{0,\Omega} \right).
\end{aligned}
$$

If we choose $k > \mathrm{Re}\, C_{1,h} ||\boldsymbol{g}||_{0,\Omega}$, then for $||\boldsymbol{v}_h||_{x_2} = k$, $(f(\boldsymbol{v}_h), \boldsymbol{v}_h)_{x_2} > 0$. As a result, the lemma 1.4 p.164 in [24] ensures the existence of a solution $\boldsymbol{u}_h$ of the equation $f(\boldsymbol{u}_h) = 0$, in other words, a solution of the discrete problem (22). $\square$

Remark. For the inequality (33), a better majoration can be given in the case $g_2 = 0$. Indeed, from the Cauchy-Schwarz inequality and the Poincaré inequality, we have:

$$\forall \boldsymbol{v}_h \in \boldsymbol{H}_{h,b}, \quad |(\boldsymbol{g}, \boldsymbol{v}_h)_\Omega| \leq C(\Omega) ||g_1||_{0,\Omega} \, ||\boldsymbol{v}_h||_{x_2}. \tag{34}$$

Hence, if we define $k_0 = (\operatorname{Re} C(\Omega) ||g_1||_{0,\Omega})$, the Lemma 1.4 in [24] also ensures that $||\boldsymbol{u}_h||_{x_2} \leq k_0$, thus $||u_{h,1}||_{0,\Omega} \leq C(\Omega) k_0$, using again the Poincaré inequality. In other words, the set $\{||u_{h,1}||_{0,\Omega}\}_{(h>0)}$ is bounded. $\square$

For the problem (23), we now have the following lemma:

Lemma 3. *The pair $\mathbb{P}_2/\mathbb{P}_1/\mathbb{P}_0$ is inf-sup stable, i.e., there exists a constant $\beta > 0$, independent of h, such that:*

$$\inf_{q_h \in \Pi_h} \sup_{\boldsymbol{v}_h \in \boldsymbol{H_h}} \frac{b(q_h, \boldsymbol{v}_h)}{||\boldsymbol{v}_h||_{\boldsymbol{H}(\Omega)}||q_h||_{0,\Omega}} \geq \beta. \tag{35}$$

Then, for a given $\boldsymbol{u}_h$, the problem (23) admits one unique solution $p_h \in \Pi_h$.

Proof. In [23] it is proved that

$$\inf_{q_h \in \Pi_h} \sup_{\boldsymbol{v}_h \in \boldsymbol{H_h}} \frac{b(q_h, \boldsymbol{v}_h)}{||\boldsymbol{v}_h||_{1,\Omega}||q_h||_{0,\Omega}} \geq \beta, \tag{36}$$

and the result arises from (9). $\square$

Collecting the previous results, we can state the main theorem of this section:

Theorem 1. *The problem (22)-(23) admits at least one solution $(\boldsymbol{u}_h, p_h)$. Furthermore, in the case of $g_2 = 0$, the set $\{||u_{h,1}||_{0,\Omega}\}_{(h>0)}$ is bounded by $(C(\Omega)^2 \operatorname{Re} ||g_1||_{0,\Omega})$, where $C(\Omega)$ is the constant from the Poincaré inequality.*

Remark :

(1) For the Taylor-Hood element and the Mini element, the inf-sup condition is also valid, which ensures that the discrete problem (23) has a unique solution for a given $\boldsymbol{u}_h$. Nevertheless, for these elements, and $\lambda = 0$, the problem (22) might have no solution. Indeed, Lemma 2 might not be valid since for these elements, $||.||_{x_2}$ might not be a norm on $\boldsymbol{H_{h,b}}$ (note that the specific properties of the $\mathbb{P}_2/\mathbb{P}_1/\mathbb{P}_0$ element have been used in the proof of Lemma 1). This has been confirmed by the numerical experiments that fail for these elements.

(2) Note that no majoration of the transverse velocity $u_{h,2}$ has been provided. This is due to the very particular nature of the RNS/P equations, that allow a weak control on this variable.

3.4 Description of the algorithm of resolution

For numerical simulations, boundary conditions that are not homogeneous have been considered (see equation (3) and remark below equation (12)). For the inlet flow, a Poiseuille profile has been chosen:

$$u_1^0(x_2) = 4(1 - x_2)x_2. \tag{37}$$

The Newton method has been used to deal with the non-linearity that arises from the convective term. At each step of the Newton loop, the linearized discrete problem is solved using a

9

multi-frontal Gauss LU factorization (cf. [10]) implemented in the package `UMFPACK`[4] (cf. [9]). The complete scheme of the numerical resolution is given in Fig. 2.

The first numerical parameter is λ, which is the coefficient for the least-squares term $a_\lambda(\cdot, \cdot)$. It has been chosen for the numerical experiments as a constant and not as a scalar function. The two other parameters are n_{Re} and ε_N which are respectively the number of steps in the continuation loop 1 and the convergence criterion for the Newton loop. This latter has been fixed to 10^{-7} for all the simulations. The convergence in the Newton loop has been measured through computation of:

$$||(\boldsymbol{du}_h, dp_h)||_{\max} = \max_{\mathcal{T}_h} ||(\boldsymbol{du}_h, dp_h)||_2, \tag{38}$$

where $(\boldsymbol{du}_h, dp_h)$ is the increment in each iteration, defined in Fig. 2. All the numerical results have been obtained using FreeFEM++ software [14].

4   Numerical results and discussion

The problem consists of computing the fluid flow in a constricted pipe, a type of geometry which corresponds to a great variety of situations: flow in a Venturi pipe [25], in a collapsible tube [6], in a stenosis [3], in the vocal folds [20] or in the human pharynx [22], etc. The geometry can either be symmetric (for instance in a stenosis) or asymmetrical (for instance in the human pharynx or at the base of the tongue). Here, we have considered the asymmetrical problem. The characteristics of one representative simplified geometry are given in Fig. 3: it is a straight pipe which is constricted because of a bump in the upper border. The pertinent parameters for this type of problem are the width δ and the height h_b of the bump, as well as the Reynolds number Re.

The simulations have been carried out for three types of geometries:

− *(geometry 1)* A long pipe with a slightly curved upper wall ($\delta = 5$, $h_b = 0.2$). It corresponds to an ideal case in which the assumptions of validity of the RNS/P equations should be encountered.
− *(geometry 2)* A pipe with a small obstacle ($\delta = 0.1$, $h_b = 0.2$), a case described in [16]. It permits to test the method in a more realistic situation, with separation of the flow above a given Reynolds number.
− *(geometry 3)* A severe constriction ($\delta = 0.5$, $h_b = 0.5$), a case described in [17]. The interest is to test the method and the model itself in a situation corresponding to the limit of validity of the RNS/P equations.

The meshes for each case are depicted Fig. 4. The range for the Reynolds number Re is $1 - 1000$ for the geometry 1, $1 - 500$ for the geometry 2 and $1 - 100$ for the geometry 3. In a first set of experiments, the value for λ has been fixed to 0. For comparison, the complete Navier-Stokes equations have been solved, on the same geometry and with the same mesh.

---

[4] *http://www.netlib.org/linalg*

The numerical strategy is the same as for RNS/P equations: a continuation method with a Newton loop to treat the non-linearity. The number of steps of the continuation method is always the same for Navier-Stokes and RNS/P. The convergence criterion ε_N for the Newton loop is fixed to the same value as for the RNS/P equations: 10^{-7}. For discretization, $\mathbb{P}_2/\mathbb{P}_1$ Taylor-Hood elements have been considered (quadratic interpolation on the velocity and linear interpolation on the pressure) [11]. No stabilization of the finite element approximation has been used in the convection-dominated regime, since no pure oscillations have been observed in the numerical solutions. The pressure drop ΔP between the inlet and the outlet, which is an output of the simulations, has been compared. Moreover, the force $\boldsymbol{F}_{\mathrm{sup}}$ exerted by the fluid on the upper wall has been computed since it is of particular interest in the case of fluid-structure interaction. This force is defined as

$$\boldsymbol{F}_{\mathrm{sup}} = \int_{\Gamma_{\mathrm{sup}}} \boldsymbol{\sigma}_f \boldsymbol{n} \, \mathrm{d}\Gamma, \tag{39}$$

where Γ_{sup} is the upper part of the boundary, $\boldsymbol{\sigma}_f$ is the tensor of fluid constraints and $\boldsymbol{n}$ is the inner unit vector normal to the boundary. It is of interest to decompose $\boldsymbol{F}_{\mathrm{sup}}$ as:

$$\boldsymbol{F}_{\mathrm{sup}} = \boldsymbol{F}^p_{\mathrm{sup}} + \frac{1}{\mathrm{Re}} \boldsymbol{F}^\tau_{\mathrm{sup}}, \tag{40}$$

where $\boldsymbol{F}^p_{\mathrm{sup}}$ is the contribution of the pressure:

$$\boldsymbol{F}^p_{\mathrm{sup}} = \int_{\Gamma_{\mathrm{sup}}} (-p\,\boldsymbol{n}) \, \mathrm{d}\Gamma, \tag{41}$$

and $\boldsymbol{F}^\tau_{\mathrm{sup}}$ is the contribution of the shear stress:

$$\boldsymbol{F}^\tau_{\mathrm{sup}} = \int_{\Gamma_{\mathrm{sup}}} (\nabla \boldsymbol{u} + \nabla \boldsymbol{u}^{\mathrm{T}}) \boldsymbol{n} \, \mathrm{d}\Gamma. \tag{42}$$

In practice, for incompressible flows, the contribution from the shear stress is negligible with respect to the contribution from the pressure (see e.g. [8]). The results of the computations and of the comparisons (pressure drop ΔP and quadratic norms of $\boldsymbol{F}_{\mathrm{sup}}$, $\boldsymbol{F}^p_{\mathrm{sup}}$, $\boldsymbol{F}^\tau_{\mathrm{sup}}$) are presented in Table 1.

For the geometry 1 and for a Reynolds number of 1000, the pressure distribution p and the horizontal velocity u_1 are depicted Fig. 5. The predictions of ΔP and $\boldsymbol{F}_{\mathrm{sup}}$ are in good adequation with those from the Navier-Stokes simulations, taken as a reference. The maximal error is found for Re = 1000, and is of 2 % for ΔP and of 8 % for $\boldsymbol{F}_{\mathrm{sup}}$. This error corresponds to the quantity

$$\frac{|\Delta P_{\mathrm{NS}} - \Delta P_{\mathrm{RNS/P}}|}{\Delta P_{\mathrm{NS}}}, \tag{43}$$

where NS indicates the prediction from Navier-Stokes simulations and RNS/P the prediction from RNS/P simulations (the same computation is done for $\boldsymbol{F}_{\mathrm{sup}}$). As a result, the simulations for this geometry have permitted to validate the numerical method.

For the geometry 2 and Re = 100, the pressure distribution p and the horizontal velocity u_1 are depicted in Fig. 6. For Re = 1, the prediction of ΔP and $\boldsymbol{F}_{\sup}$ corresponds to the prediction from Navier-Stokes simulations, with errors of 6 % and 1.5 %, respectively. When the Reynolds number Re is 100, and the convection such that recirculation effects are observed behind the obstacle in Navier-Stokes simulations, the prediction of ΔP and $\boldsymbol{F}_{\sup}$ remains satisfying (errors of 9 % and 2 % respectively), though the RNS/P equations are in principle not adapted for the simulation of recirculation effects, because of the assumption $\partial_{x_2} p = 0$. The reason is that in this case, the global effect of recirculation is weak. Note however that the pressure distribution at the level of the bump differs between RNS/P and Navier-Stokes. Though the drop is approximatively of the same magnitude, it is anticipated in the RNS/P simulation, with an abrupt pressure recovery that is not present in the Navier-Stokes simulation. Note also that the effects of recirculation affect the values of the velocity and therefore the value of $\boldsymbol{F}_{\sup}^{\tau}$, which is different between RNS/P and Navier-Stokes simulations (error of 37.5 %). For a Reynolds number Re of 500, the recirculation is stronger. This does not prevent the RNS/P simulation to converge but the results are quite different from those of the Navier-Stokes simulation: an error of 24 % for ΔP and an error of 36 % for $\boldsymbol{F}_{\sup}$.

For the geometry 3 and Re = 1, p and u_1 are depicted Fig. 7. The adequation between RNS/P and Navier-Stokes simulations is still satisfying for Re = 1, with an error of 13.5 % for ΔP and an error of 8 % for $\boldsymbol{F}_{\sup}$. This is slightly higher than in the precedent cases, but this fact is somehow expected since for this kind of geometry the RNS/P equations are in their limit of validity. Due to the recirculation effects, the error is more important when Re is increased to 50 or 100, and is up to 23 % for ΔP and 21 % for $\boldsymbol{F}_{\sup}$ (for Re = 100).

Computing times[5] for each simulation are indicated in Table 1 for $\lambda = 0$. It appears from the results that for Re $\gg$ 1, the RNS/P simulations are faster than the NS simulations, of approximatively 30 %. This gain comes from the fact that less Newton iterations are required with RNS/P to reach the same convergence criterion. In the case Re = $O(1)$, the computing time for RNS/P is comparable to the computing time for NS, except for the geometry 3 in which it is higher for RNS/P. This might be due to the linear system which should be ill-conditioned for small Reynolds. This case is however not physically relevant, as the RNS/P equations have been designed for flows with high Reynolds number.

The influence of the least-squares term $a_\lambda(\cdot, \cdot)$ has finally been assessed. Simulations have been carried out with $\lambda = 1$ for the geometries 1 and 2. Simulations with the geometry 1 reveal the first interest of this least-squares term: it decreases significantly the computing time. Indeed, a speed-up of approximatively 2 is achieved in comparison to the reference simulations with Navier-Stokes (see Table 2). This term has in particular two effects: it makes easier the resolution of the linear system at each iteration, and it decreases the number of Newton iterations at each continuation step. Of course, for this geometry, this term does not improve the accuracy since results were already very close to those obtained from Navier-Stokes when λ was fixed to 0. Simulations for the geometry 2 also confirm these considerations on the computing time (see Table 3). The role of simulations on this geometry is then to show the other interest of the

---

[5] The computer on which simulations have been carried out is a Power PC G4 1.2 GHz, with RAM of 256 MO.

term $a_\lambda(\cdot, \cdot)$: it may improve the performance of prediction. For this geometry and Re ≤ 100, the results are very close to the ones obtained with $\lambda = 0$, so that the difference with the Navier-Stokes simulations is nearly the same. Concerning the prediction of the shear stress component $\boldsymbol{F}_{\text{sup}}^\tau$ at Re = 100, the results are better with $\lambda = 1$, as the error is of 15 % instead of the 37.5 % mentioned previously for $\lambda = 0$. For Re > 100, the results presented in Table 3 show clearly that the performance of prediction is improved with $\lambda = 1$. Concerning ΔP, the error is of 7.5 % for $\lambda = 1$ instead of 14 % for $\lambda = 0$ when Re = 200 (respectively, 6 % and 24 % when Re = 500). For $\boldsymbol{F}_{\text{sup}}$, the error decreases from 5 % to 2 % when λ changes from 0 to 1, when Re = 200 (respectively from 36 % to 15 % when Re = 500). Indeed, when the Reynolds number is high and the convection effects become predominant in the fluid, the least-square term allows an *ad-hoc* reproduction of the recirculation behind the obstacle, though underestimated if compared to those observed in the Navier-Stokes simulations (see Fig. 8). This explains the better estimation of $\boldsymbol{F}_{\text{sup}}^\tau$ (see Table 3) and $\boldsymbol{F}_{\text{sup}}$ in particular.

As the choice $\lambda = 1$ is of course not the only possible, a sensitivity study has been carried out, which results are presented in Table 4. First, we noted that the value of this parameter has not a significant impact on the computing time when it is chosen different from 0: for $\lambda \geq 1$, this time remained to be 1'21 (1'44 for $\lambda = 0$). Nevertheless, concerning the performance of prediction, the value of $\lambda = 2$ is the optimal for $\boldsymbol{F}_{\text{sup}}$ (0.6 % of error) and $\lambda = 3$ is the optimal for ΔP (0.7 % of error), so a value of λ between 2 and 3 should be the best for carrying out simulations. Though increasing λ reduces the error on $\boldsymbol{F}_{\text{sup}}^\tau$, it increases the error on ΔP and $\boldsymbol{F}_{\text{sup}}$ if $\lambda > 3$, so values of λ greater than 3 might not be a good choice.

5   Concluding remarks

A finite element method to solve the Reduced Navier-Stokes/Prandtl (RNS/P) equations has been described and tested. The discretization is based on an element originally defined in [23] for the Stokes equations. With this element, called $\mathbb{P}_2/\mathbb{P}_1/\mathbb{P}_0$, the velocity is approximated with continuous piecewise quadratic and linear functions, while the pressure is approximated with a piecewise constant function. This element, as Taylor-Hood and the Mini element, verifies the inf-sup condition for the RNS/P equations. However, the subproblem of computing the discrete velocity $\boldsymbol{u}_h$ might be ill-posed for the Taylor-Hood and the Mini element, which systematically leaded to failures in the numerical experiments. In opposite, we show that with the proposed $\mathbb{P}_2/\mathbb{P}_1/\mathbb{P}_0$ element, this subproblem admits a solution. Furthermore, it was shown that the longitudinal component of $\boldsymbol{u}_h$ is bounded by a constant independent of h, the parameter of discretization.

Numerical experiments permitted to test the method for some particular geometries, and to show that the prediction of the pressure drop and of the constraints on the surrounding walls is comparable to the prediction from Navier-Stokes simulation. Moreover, the current method avoids limitations of the precedent finite differences method used for instance in [15], which lacks of adaptivity for some geometries and for coupling with other physical entities, such as a moving wall. Also, a bidimensional problem has been chosen for the simplicity of the presentation, but the extension to three-dimensional geometries is straightforward. Even in the case of moderate recirculation effects (small obstacle in a duct for instance), the method still gives

a correct approximation of the predicted variables, whereas in the finite difference context, the computation had to be stopped, and only a prediction of the pressure and of the velocity on the upstream part of the domain was provided [17]. In the case of strong recirculation, for instance in a severe constriction, both finite differences and finite elements are unsatisfying. However, in this case, the RNS/P equations are out of their domain of validity, and a Navier-Stokes solver should be used instead for an accurate simulation.

Concerning the performance of the method, a gain has been observed systematically in comparison with Navier-Stokes simulation. The reason is that less Newton iterations are required to reach convergence with the RNS/P equations. Moreover, the least-squares stabilization term has a positive impact on the speed-up, by its effect on the resolution of the linear system at each Newton iteration, and as it decreases even more the number of Newton iterations. In addition, this gain should be increased significantly, more specifically in the three-dimensional case, by improving the method for the resolution of the linear system which is built at each iteration. For instance, it would be interesting to design preconditioners adapted to this system. Another possibility would consist in implementing and studying the effect of stabilization techniques much more sophisticated than the simple one that has been used (see e.g. [12] for the Navier-Stokes case). These two points will be object of future research.

Another perspective concerns shallow water flows, for which the Navier-Stokes equations are simplified in a very similar manner [1, 2]. Nevertheless, the term $\partial_{x_1^2}^2 u_1$ is conserved in the laplacian, though it is not justified asymptotically. Thus, it would be interesting to study the applicability of the proposed method to shallow water equations. The last perspective is the extension of this finite element method to a coupled fluid/structure interaction problem and to three-dimensional geometries.

Acknowledgements

References

1. P. Azérad. *Analyse des équations de Navier-Stokes en bassin peu profond et de l'équation de transport*. PhD thesis, Université de Neuchâtel, Neuchâtel, Switzerland, 1996.
2. P. Azérad and F. Guillén. Mathematical justification of the hydrostatic approximation in the primitive equations of geophysical fluid dynamics. *SIAM Journal of Mathematical Analysis*, 33(4):847–859, 2001.
3. S.A. Berger and L-D Jou. Flows in stenotic vessels. *Annual Review of Fluid Mechanics*, 32:347–382, 2000.
4. M. Braack, E. Burman, V. John, and G. Lube. Stabilized finite element methods for the generalized Oseen problem. *Comput. Methods Appl. Mech. Engrg.*, 196:853–866, 2007.
5. W.R. Briley. Numerical method for predicting three-dimensional steady viscous flow in ducts. *Journal of Computational Physics*, 14:8–28, 1974.
6. P.W. Carpenter and T.J. Pedley, editors. *Flow in collapsible tubes and past other highly compliant boundaries*, chapter 2. Flows in Deformable Tubes and Channels. Theoretical Models and Biological Applications (M. Heil and O.E. Jensen), pages 15–49. Kluwer, 2003.

7. A.J. Chorin and J.E Mardsen. *A Mathematical Introduction to Fluid Mechanics - Third Edition*. Springer-Verlag, 1993.

8. F. Chouly, A. Van Hirtum, P.-Y. Lagrée, X. Pelorson, and Y. Payan. Numerical and experimental study of expiratory flow in the case of major upper airway obstructions with fluid-structure interaction. *Journal of Fluids and Structures*, 24:250–269, 2008.

9. T.A. Davis. Algorithm 832: UMFPACK V4.3- an unsymmetric-pattern multifrontal method. *ACM Trans. Math. Software*, 30:196–199, 2004.

10. T.A. Davis and I.S. Duff. A combined unifrontal/multifrontal method for unsymmetric sparse matrices, 1999. Technical Report 20, CISE, University of Florida.

11. A. Ern and J.-L. Guermond. *Theory and Practice of Finite Elements*. Springer-Verlag, 2004.

12. L. P. Franca and S. L. Frey. Stabilized finite element methods. II. The incompressible Navier-Stokes equations. *Comput. Methods Appl. Mech. Engrg.*, 99(2-3):209–233, 1992.

13. P.M Gresho and R.L. Sani. *Incompressible Flow and the Finite Element Method*. John Wiley & Sons, 2000.

14. F. Hecht, O. Pironneau, A. Le Hyaric, and K. Ohtsuka. Freefem++ 2.16-1 documentation, 2007. Webpage: http://www.freefem.org/ff++.

15. P.-Y. Lagrée, E. Berger, M. Deverge, C. Vilain, and A. Hirschberg. Characterization of the pressure drop in a 2D symmetrical pipe: some asymptotical, numerical and experimental comparisons. *ZAMM - Journal of Applied Mathematics and Mechanics*, 85(2):141–146, 2005.

16. P.-Y. Lagrée and S. Lorthois. The RNS/Prandtl equations and their link with other asymptotic descriptions: application to the wall shear stress scaling in a constricted pipe. *International Journal of Engineering Science*, 43:352–378, 2005.

17. P.-Y. Lagrée, A. Van Hirtum, and X. Pelorson. Asymmetrical effects in a 2D stenosis. *European Journal of Mechanics B/Fluids*, 26:83–92, 2007.

18. P.A. Raviart and J.M. Thomas. *Introduction à l'Analyse Numérique des Équations aux Dérivées Partielles*. Masson, 1992.

19. T.-A. Reyhner and Flügge-Lotz. The interaction of a shockwave with a laminar boundary layer. *International Journal of Non-Linear Mechanics*, 3:173–199, 1968.

20. R.-C. Scherer, D. Shinwari, K.-J. De Witt, C. Zhang, B.-R. Kucinschi, and A.-A. Afjeh. Intraglottal pressure profiles for a symmetric and oblique glottis with a divergence angle of 10 degrees. *Journal of the Acoustical Society of America*, 109:1616–1630, 2001.

21. H. Schlichting. *Boundary-layer theory*. McGraw-Hill Publishing Company, 1979.

22. B. Shome, L.-P. Wang, M.-H. Santare, A.-K. Prasad, A.-Z. Szeri, and D. Roberts. Modeling of airflow in the pharynx with application to sleep apnea. *Journal of Biomechanical Engineering*, 120:416–422, 1998.

23. R. Stenberg. Error analysis of some finite element methods for the Stokes problem. *Mathematics of Computation*, 54:495–508, 1990.

24. R. Temam. *Navier-Stokes Equations*. North-Holland, Elsevier, 1985.

25. S. Turek. *Efficient Solvers for Incompressible Flow Problems. An Algorithmic and Computational Approach*. Springer, 1999.

26. A. Van Hirtum, X. Pelorson, and P.-Y. Lagrée. In vitro validation of some flow assumptions for the prediction of the pressure distribution during obstructive sleep apnea. *Medical & Biological Engineering & Computing*, 43:162–171, 2005.

27. O.E. Zienkiewicz, R.L. Taylor, and P. Nithiarasu. *The Finite Element Method for Fluid Dynamics - Sixth Edition*. Butterworth-Heinemann, 2005.

geometry	Re	ΔP	$\|\boldsymbol{F}_{\text{sup}}\|$	$\|\boldsymbol{F}^p_{\text{sup}}\|$	$\|\boldsymbol{F}^\tau_{\text{sup}}\|$	time
	1	215.4	2218.0	2216.8	96.6	0'36
(1)	100	2.16	20.80	20.79	96.6	0'45
	500	0.46	3.51	3.51	97.6	2'07
	1000	0.26	1.62	1.62	100.1	3'29
	1	40.98	105.14	103.03	21.92	0'45
(2)	100	0.42	1.03	0.99	21.87	1'03
	500	0.10	0.17	0.17	20.81	4'16
	1	71.33	157.66	150.72	31.96	1'16
(3)	50	1.53	2.53	2.48	31.38	1'03
	100	0.85	0.94	0.94	30.95	4'32

geometry	Re	ΔP	$\|\boldsymbol{F}_{\text{sup}}\|$	$\|\boldsymbol{F}^p_{\text{sup}}\|$	$\|\boldsymbol{F}^\tau_{\text{sup}}\|$	time
	1	216.1	2174.8	2173.6	97.1	0'41
(1)	100	2.16	20.36	20.35	97.0	1'12
	500	0.46	3.38	3.37	98.0	2'53
	1000	0.25	1.51	1.50	100.3	5'10
	1	43.52	106.66	105.66	18.55	0'40
(2)	100	0.46	1.01	1.00	15.91	1'23
	500	0.13	0.13	0.12	9.41	6'15
	1	82.47	171.20	165.16	26.58	0'38
(3)	50	1.85	2.92	2.90	24.35	1'30
	100	1.10	1.19	1.19	21.16	6'20

Table 1. Results of the computations for the RNS/P equations (left) and the full Navier-Stokes equations (right). The pressure difference and the force on the superior wall are indicated, as well as the computing time (in minutes/seconds) of the simulations.

equations	ΔP	$\|\boldsymbol{F}_{\text{sup}}\|$	$\|\boldsymbol{F}^p_{\text{sup}}\|$	$\|\boldsymbol{F}^\tau_{\text{sup}}\|$	time
Navier-Stokes	1.09	9.58	9.56	97.04	1'32
RNS/P ($\lambda = 0$)	1.09	9.81	9.79	96.61	1'10
RNS/P ($\lambda = 1$)	1.09	9.79	9.77	96.95	0'40

equations	ΔP	$\|\boldsymbol{F}_{\text{sup}}\|$	$\|\boldsymbol{F}^p_{\text{sup}}\|$	$\|\boldsymbol{F}^\tau_{\text{sup}}\|$	time
Navier-Stokes	0.46	3.38	3.37	98.0	2'53
RNS/P ($\lambda = 0$)	0.46	3.51	3.51	97.6	2'07
RNS/P ($\lambda = 1$)	0.46	3.46	3.45	97.8	1'22

Table 2. Influence of the parameter λ for simulations with the geometry 1. The Reynolds number Re is 200 (left) and 500 (right).

equations	ΔP	$\|\boldsymbol{F}_{\text{sup}}\|$	$\|\boldsymbol{F}^p_{\text{sup}}\|$	$\|\boldsymbol{F}^\tau_{\text{sup}}\|$	time
Navier-Stokes	0.25	0.46	0.45	13.79	2'44
RNS/P ($\lambda = 0$)	0.21	0.48	0.48	21.56	1'44
RNS/P ($\lambda = 1$)	0.23	0.45	0.45	16.61	1'23

equations	ΔP	$\|\boldsymbol{F}_{\text{sup}}\|$	$\|\boldsymbol{F}^p_{\text{sup}}\|$	$\|\boldsymbol{F}^\tau_{\text{sup}}\|$	time
Navier-Stokes	0.13	0.13	0.12	9.41	6'15
RNS/P ($\lambda = 0$)	0.10	0.17	0.17	20.81	4'16
RNS/P ($\lambda = 1$)	0.12	0.15	0.15	13.09	3'16

Table 3. Influence of the parameter λ for simulations with the geometry 2. The Reynolds number Re is 200 (left) and 500 (right).

λ	ΔP	$\|\boldsymbol{F}_{\text{sup}}\|$	$\|\boldsymbol{F}^p_{\text{sup}}\|$	$\|\boldsymbol{F}^\tau_{\text{sup}}\|$	time
0	14.1	5.3	5.5	56.3	1'44
1	7.5	1.7	1.1	20.4	1'23
2	3.6	0.6	0.1	13.7	1'21
3	0.7	1.3	2.2	9.8	1'20
4	1.8	3.4	4.5	7.0	1'21
5	4.3	5.5	6.9	4.9	1'21

Table 4. Study of the parameter λ for simulations with the geometry 2. The Reynolds number Re is 200. The relative error in % in comparison to Navier-Stokes simulations is given for each variable.

Init:

- Read the simulation parameters and the mesh.
- Init the velocity and the pressure: $(\boldsymbol{u}_h, p_h)$.
- Init the Reynolds number Re.

Loop 1: Continuation strategy.

- **Loop 2:** Newton iteration.

  - Solve the linearized problem:

    Find $(\boldsymbol{du}_h, dp_h)$ such that

$$
\begin{cases}
\forall \boldsymbol{v}_h, \\
\quad c_{\mathrm{a}}(\boldsymbol{u}_h, \boldsymbol{du}_h, \boldsymbol{v}_h) + c_{\mathrm{a}}(\boldsymbol{du}_h, \boldsymbol{u}_h, \boldsymbol{v}_h) + \\
\qquad a(\boldsymbol{du}_h, \boldsymbol{v}_h) - (dp_h, \nabla \cdot \boldsymbol{v}_h)_\Omega \\
\qquad\qquad = \\
\qquad\qquad (\boldsymbol{g}, \boldsymbol{v}_h)_\Omega - c_{\mathrm{a}}(\boldsymbol{u}_h, \boldsymbol{u}_h, \boldsymbol{v}_h) \\
\qquad\qquad - a(\boldsymbol{u}_h, \boldsymbol{v}_h) + (p_h, \nabla \cdot \boldsymbol{v}_h)_\Omega, \\
\\
\forall q_h, \quad -(q_h, \nabla \cdot \boldsymbol{du}_h)_\Omega = (q_h, \nabla \cdot \boldsymbol{u}_h)_\Omega.
\end{cases}
$$

  - Update the velocity and the pressure:

$$
\boldsymbol{u}_h \leftarrow \boldsymbol{u}_h + \boldsymbol{du}_h
$$
$$
p_h \leftarrow p_h + dp_h
$$

- **End Loop 2.**

- Increase the Reynolds number Re.

End Loop 1.

End.

Fig. 2. The complete algorithm of numerical solving of the RNS/P equations.

(a)
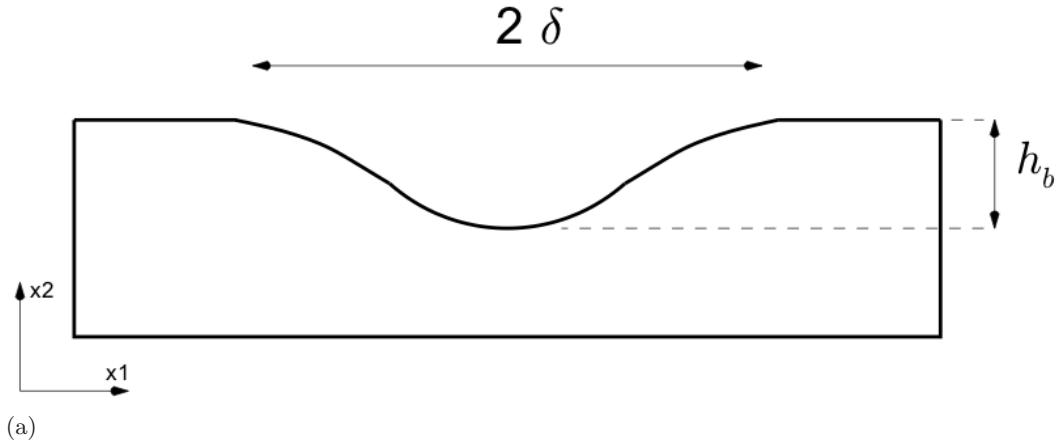
**Fig. 3.** The asymmetrical constricted pipe.

(a)
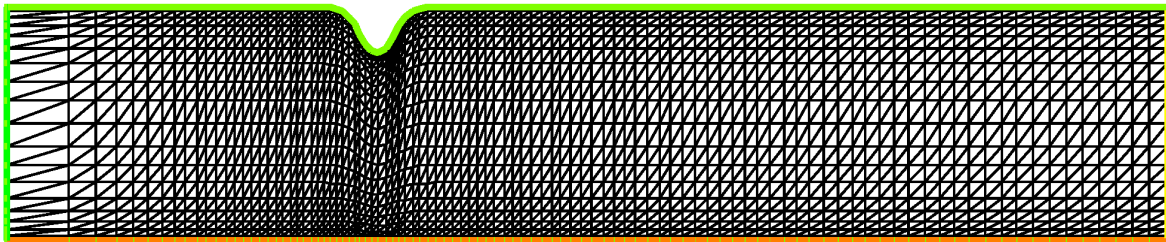
(b)
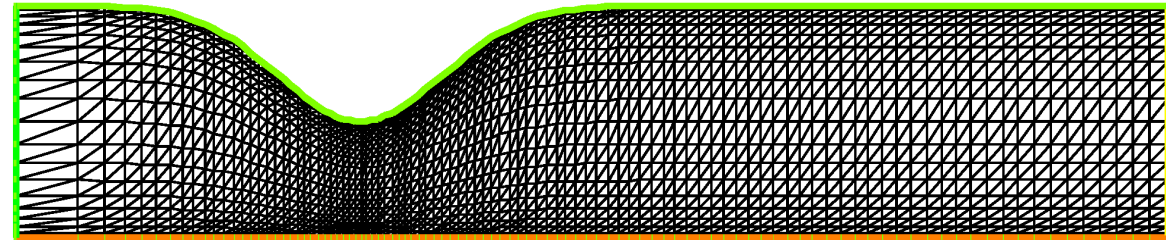
(c)

Fig. 4. The finite element meshes for the three fluid flow problems.

(a)
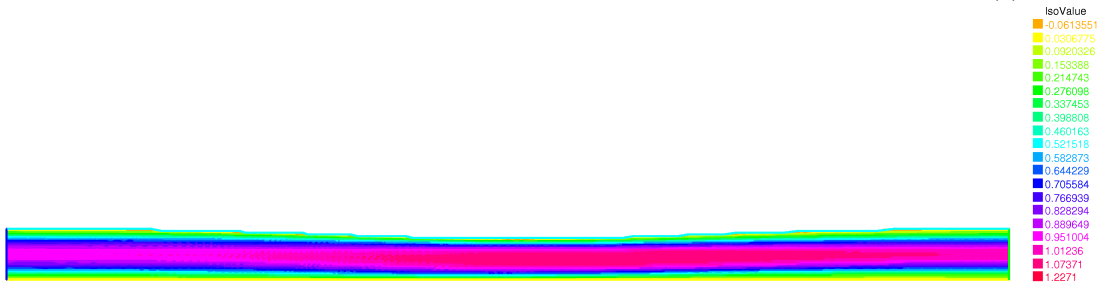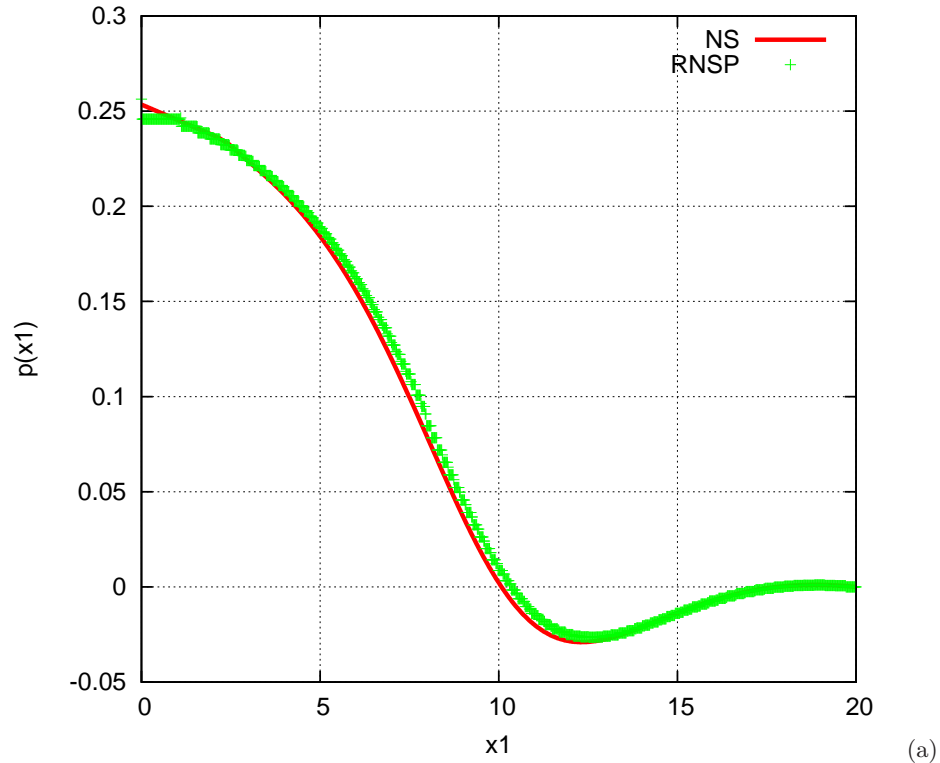
(b)

Fig. 5. Fluid flow in a constricted pipe. Geometry 1. Simulations with RNS/P equations and $\mathbb{P}_2/\mathbb{P}_1/\mathbb{P}_0$ elements. $Re = 1000$. $\lambda = 0$. Are depicted: (a) the pressure distribution p (comparison with Navier-Stokes equations), (b) the horizontal velocity u_1.

(a)

(b)
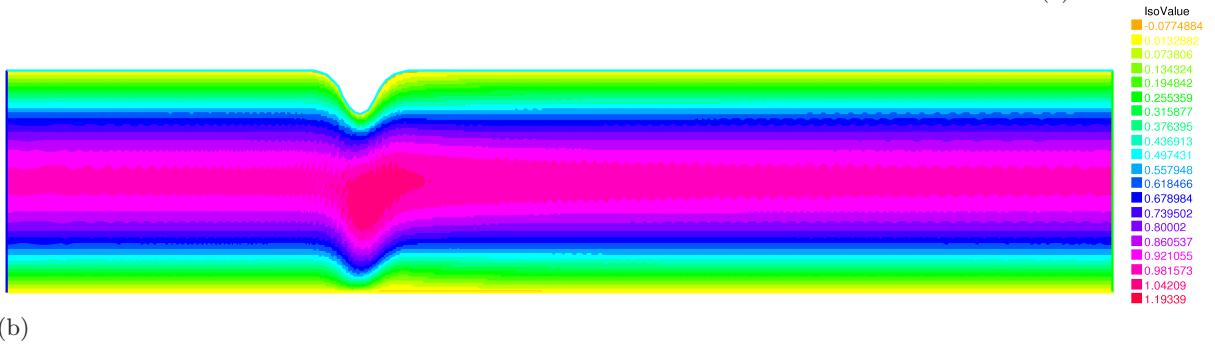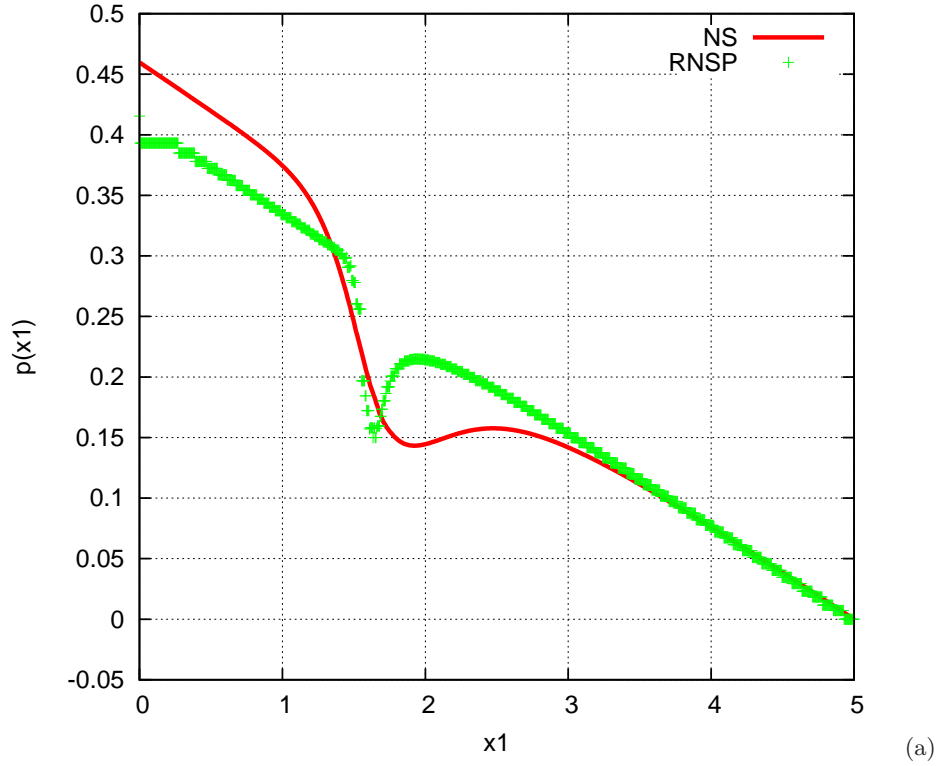
Fig. 6. Fluid flow in a constricted pipe. Geometry 2. Simulations with RNS/P equations and $\mathbb{P}_2/\mathbb{P}_1/\mathbb{P}_0$ elements. $Re = 100$. $\lambda = 0$. Are depicted: (a) the pressure distribution p (comparison with Navier-Stokes equations). (b) the horizontal velocity u_1.
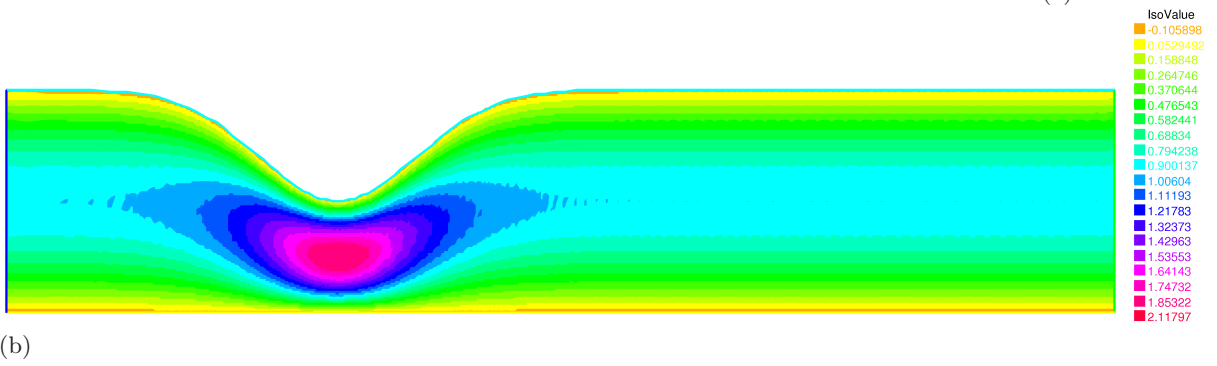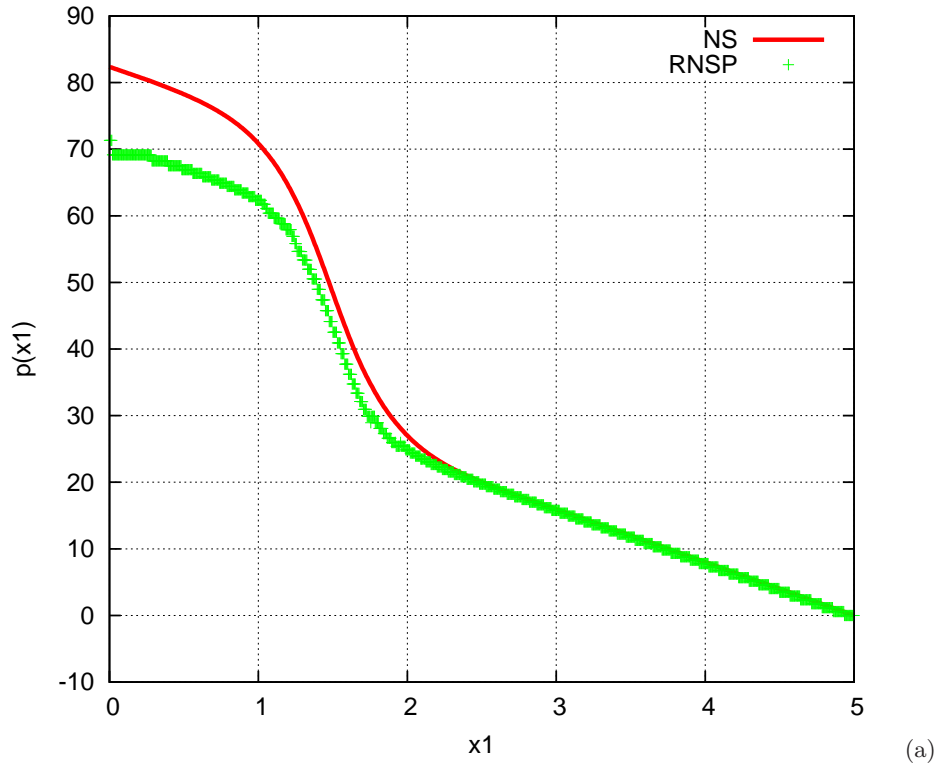
Fig. 7. Fluid flow in a constricted pipe. Geometry 3. Simulations with RNS/P equations and $\mathbb{P}_2/\mathbb{P}_1/\mathbb{P}_0$ elements. $Re = 1$. $\lambda = 0$. Are depicted: (a) the pressure distribution p (comparison with Navier-Stokes equations). (b) the horizontal velocity u_1.

21
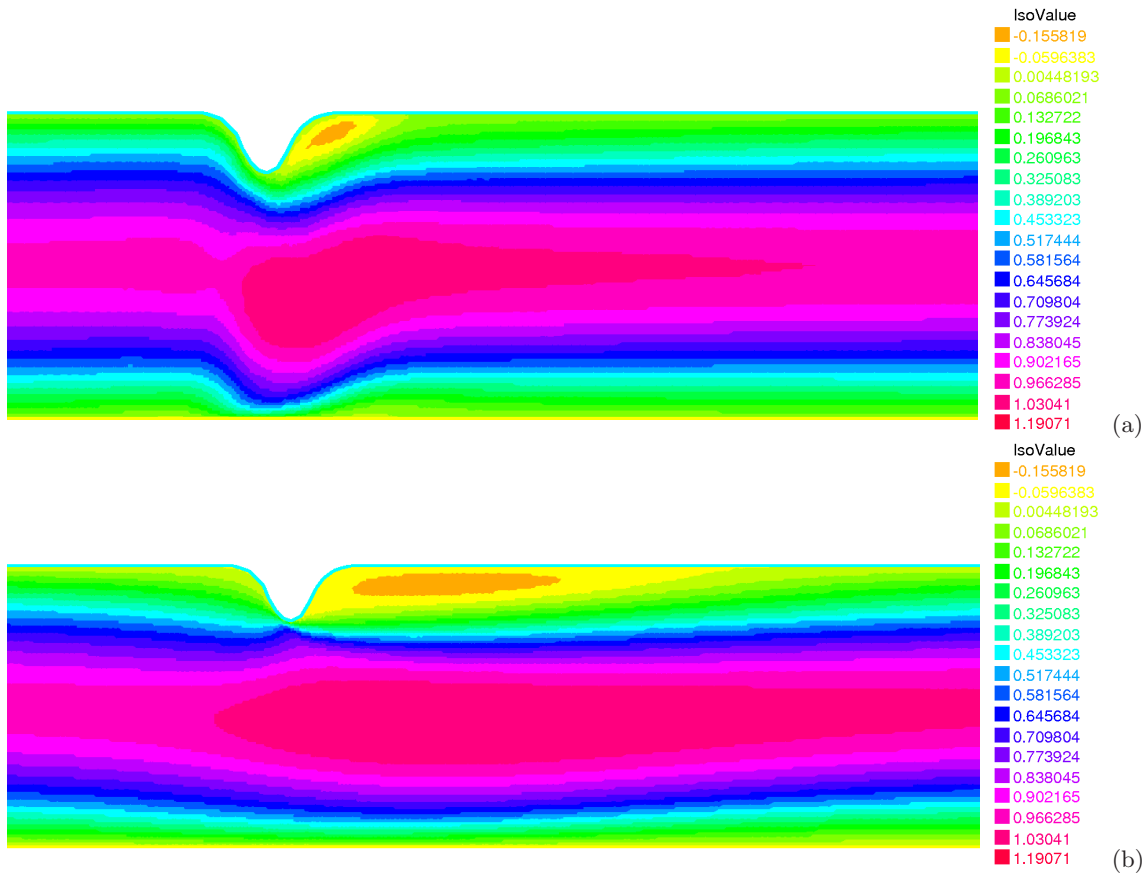
Fig. 8. Fluid flow in a constricted pipe. Geometry 2. Effect of the least-squares term $a_\lambda(\cdot, \cdot)$. $Re = 500$. $\lambda = 1$. Is depicted: the horizontal velocity u_1. (a) RNS/P simulation. (b) Navier-Stokes simulation.